Research Performance Final Report

Identification and Quantification of the Role of Turbulence in Aircraft/Ship Aerodynamics

N00014-16-1-2731
June 16, 2016 – June 30, 2021

Date Submitted:
September 30, 2021

Submitted by:
Marilyn J. Smith
Georgia Institute of Technology
(404) 894-3065
ms55@gatech.edu

and

Anya Jones
University of Maryland at College Park
(301) 405-7988
arjones@umd.edu

This work was sponsored by the Office of Naval Research (ONR), under grant (or contract) number N00014-16-1-2731. The views and conclusions contained herein are those of the authors only and should not be interpreted as representing those of ONR, the U.S. Navy or the U.S. Government.

REPORT DOCUMENTATION PAGE

PLEASE DO NOT RETURN YOUR FORM TO THE ABOVE ORGANIZATION.

1. REPORT DATE	2. REPORT TYPE	3. DATES COVERED	
		START DATE	END DATE
30-09-2021	Final Report	16-06-2016	30-06-2021

4. TITLE AND SUBTITLE

Identification and Quantification of the Role of Turbulence in Aircraft/Ship Aerodynamics

5a. CONTRACT NUMBER	5b. GRANT NUMBER	5c. PROGRAM ELEMENT NUMBER
	N00014-16-1-2731	
5d. PROJECT NUMBER	**5e. TASK NUMBER**	**5f. WORK UNIT NUMBER**

6. AUTHOR(S)

Smith, Marilyn J. and Jones, Anya R.

7. PERFORMING ORGANIZATION NAME(S) AND ADDRESS(ES)

School of Aerospace Engineering MS 0150, 270 Ferst Drive, Georgia Institute of Technology, Atlanta, GA 30332-0150

Dept. of Aerospace Engineering, 3154 Glenn L. Martin Hall, 4298 Campus Drive, Univ of MD, College Park, MD 20742

8. PERFORMING ORGANIZATION REPORT NUMBER

9. SPONSORING/MONITORING AGENCY NAME(S) AND ADDRESS(ES)	10. SPONSOR/MONITOR'S ACRONYM(S)	11. SPONSOR/MONITOR'S REPORT NUMBER(S)
Aviation, Force Projection & Integrated Defense (CODE 35) Office of Naval Research, One Liberty Center 875 North Randolph Street, Arlington, VA 22203-1995	ONR CODE 35	

12. DISTRIBUTION/AVAILABILITY STATEMENT

Unlimited, Public Release

13. SUPPLEMENTARY NOTES

14. ABSTRACT

Potential coupling of unsteady physics between ship bluff body structures and flight vehicles is present for close distances, resulting in unanticipated behavior in the vehicle and detrimental loading on the ship structures at low flight speeds and hover. This behavior can be mitigated by modifying flight speeds. Operational flight paths for unmanned aerial vehicles (UAVs) near ship superstructures should be avoided. For larger vehicles, partial immersion in these flows may result in higher pilot workload.

15. SUBJECT TERMS

Ship-Airwake Interaction; Computational Fluid Dynamics; Wind Tunnel Experiments; Turbulent Wakes

16. SECURITY CLASSIFICATION OF:			17. LIMITATION OF ABSTRACT	18. NUMBER OF PAGES
a. REPORT	b. ABSTRACT	C. THIS PAGE		
UU	UU	UU	UU	21

19a. NAME OF RESPONSIBLE PERSON	19b. PHONE NUMBER *(Include area code)*

PREVIOUS EDITION IS OBSOLETE.

STANDARD FORM 298 (REV. 5/2020)

Prescribed by ANSI Std. Z39.18

Identification and Quantification of the Role of Turbulence in Aircraft/Ship Aerodynamics

Abstract

This research provides insight into the unsteady flow physics of flight in a highly turbulent environment. It is thought that it is not necessary to numerically model turbulent scales of a flow that do not impact the aircraft and or relevant wake behavior, thereby saving computational cost, but it is of course necessary to capture those spatial and temporal scales that are significant. To date, the relevant scales have not been identified and quantitatively assessed, leading to potentially under-resolved solutions that may misinform engineering decisions, or to over-resolved solutions that may waste valuable resources. This work proffers a combined physical-numerical experimental approach to (a) identify the underlying flow physics of unsteady forcing in an interactional flow, (b) numerically model the dominant scales that impact vehicle performance across Reynolds numbers, and (c) develop an algorithm for both high and low fidelity numerical approaches. This report provides a synopsis of the grant's findings and conclusions.

Introduction

This effort is designed to provide insight into the unsteady flow physics of controlled flight in a highly turbulent environment. Flight through unsteady environments risks loss of vehicles and is a danger to pilots. It also limits the operational envelope for certain missions due to weather constraints. A better understanding of the dominant flow physics would permit improved ship design for aircraft operations, control systems for aircraft, and simulators to better train pilots.

There are many instances when an aircraft operates in the airwake of a large ship, from F-18s approaching an aircraft carrier to helicopters hovering over the flight deck of a frigate or patrol vessel, to the deployment of an unmanned vehicle. In each of these cases, aircraft must contend with the large flow structures that are shed from the structure of the ship, especially the superstructure and funnel. This unsteady flight environment is comprised of both large-scale vortical flows of a size similar in scale to the vehicle, as well as smaller scale turbulent structures shed from other hardware and antennae. There is a broad range of length scales and frequencies of unsteadiness in the flight deck area.

There has been significant work that shows that these unsteady flow structures exist,[1,2,3] and that they make aircraft operations challenging. However, there remain questions about the flow unsteadiness and its importance. Aircraft landings, hover, and take off on ships are very precise maneuvers, and the unsteadiness in the environment can be large compared to the vehicles' size and/or flight speed. The epistemic nature of local turbulence in combination with variable ship structures and operating conditions results in an intractable problem due to the formidable number of parametric variations that is possible. The problem is further complicated by the fact that it is impossible to measure these flows accurately and repeatedly in the field,[4] and full-scale Reynolds numbers are impossible to achieve in the laboratory.

Modern numerical simulation development has focused on the ability to capture more and more scales as a measure of the advancement of the state of the art, in many instances without regard to the cost and schedule limitations found in engineering organizations currently and for the foreseeable future. In addition, computations are not reliable without these details because the flow is hugely complex, with features over a large range of time and length scales. Very fine meshes are necessary to capture small-scale turbulence and very small time-steps are required to fully resolve the unsteadiness. The flow must also be modeled in three dimensions and at high Reynolds

number, further exacerbating the problem of meeting cost and schedule constraints. Thus, it is not possible to rely on computations to accurately predict all turbulent spatial and temporal scales.

These intractable limitations lead to the idea that it is not necessary to model the scales that do not impact the aircraft behavior or performance, but it is necessary to correctly capture (or model) the scales that are significant. This concept leads to some fundamental questions that need to be answered: What are the primary and secondary temporal and spatial scales of the wake of the ship superstructure that impact aircraft operation and performance? How do they vary with local atmospheric turbulence? From which ship structure(s) do they originate? What is the sensitivity of structure changes in size, shape, and location with variations in the ship speed, weather, deck motion, and ship geometry? Can these scales be adequately captured by modern CFD, and if so, what are the best practices and performance prediction errors?

The overarching goal of this project was to gain a fundamental understanding of how turbulent inflow affects aircraft performance, maneuverability, and controllability. Aircraft performance and controllability in unsteady environments is ultimately governed by the unsteady aerodynamic loading on the vehicle, and this unsteady loading is closely related to the environment in which it is operating. If the time and length scales of the inflow turbulence are sufficiently large, the flow is quasi-steady and classical analyses can be applied. Conversely, if they are very short, reaction times are too short for the implementation of flight or flow control. For some intermediate scales, however, unsteady turbulent fluctuations will be both large and controllable. The current work seeks to define this parameter space in the context of ship airwakes and evaluate to what extent the structure of the airwake can be modified to accommodate aircraft operations. Such modifications must arise from an understanding of the underlying flow physics. What flow structures are responsible for unsteady loading, and where do they originate? Identification of the relevant flow physics will inform modeling efforts, both high fidelity CFD and low-order modeling. By capturing and resolving the dominant flow physics, computational effort can be concentrated in the temporal or spatial scales, thereby making this highly complex problem tractable. Furthermore, by focusing on the physics of the problem, insight into the effect of scaling is also gained. Having identified the most relevant physics, it is then possible to assess sensitivity to Reynolds number and other flow parameters. Schematics of the test configurations are illustrated in Figure 1.

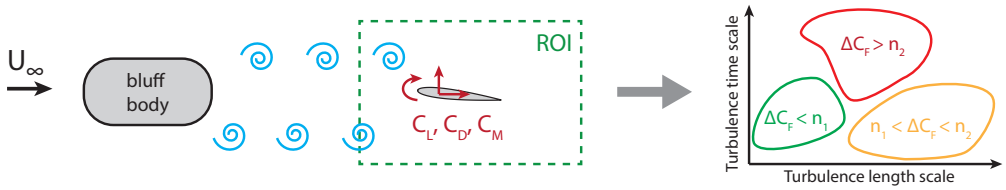

a) Bluff body turbulent wake characteristic assessment (Tasks 1 and 3)

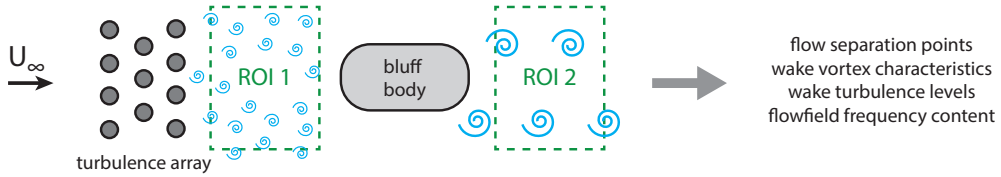

b) Bluff body turbulent wake in a turbulent inflow characteristic assessment (Tasks 2 and 3)

Figure 1: Graphical description of the canonical wind tunnel and numerical experiments.

Specifically, this research project had the following technical major goals/objectives pertinent to relevant Naval Technology Focus Areas:

- Identification and quantification of the impact of different scales of turbulence on the integrated performance quantities of Naval vehicles (ships) and their wake structures.
- Advancement of current understanding of the correct simulation level (LES, URANS, URANS/LES) that is sufficient to capture turbulent scales of interest for performance and wake analyses, along with best practices for their use.
- Scaling and application of laboratory-scale results to full-scale Naval applications.
- An exploration of new algorithms to enhance the ability to accurately capture turbulence impacts in flight simulations.

Experimental Methodology

Wind tunnel experiments were performed at the University of Maryland using an open-circuit, low speed wind tunnel with a maximum freestream velocity of 135 mph (60 m/s). The wind tunnel has a 20×28×45 inch test section. A NACA 0012, with a chord c of 2.8 in and span of 19.9 in, was placed downstream of a cylinder, as shown in Figure 2. The distance between the test objects was measured from the cylinder trailing edge to the airfoil leading edge. The airfoil location was held constant whereas the cylinder could be relocated in between test runs. Both test model geometries were selected due to the abundance of publicly available data. Four different parameters were studied during the wind tunnel experiments, including three Reynolds numbers based on airfoil chord, five cylinder streamwise locations, various airfoil angles of attack (−20 to +20 degrees), and three cylinder diameters. The test matrix is summarized in Table 1.

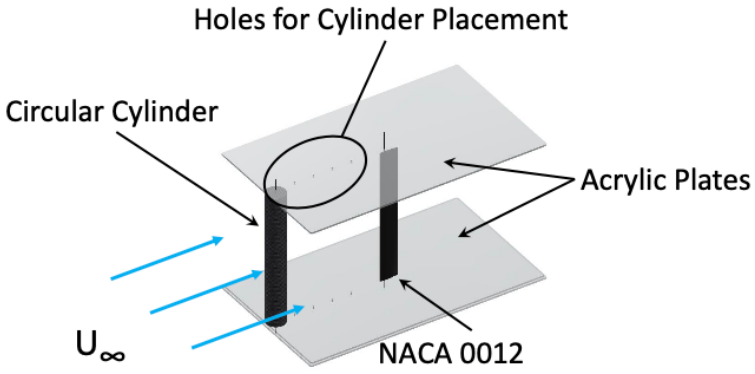

Figure 2: Wing and circular cylinder in wind tunnel test section.

Table 1: Force measurements test matrix.

Cylinder diameter, D/c	$\mathrm{Re_c}$	α, deg	Cylinder-airfoil distance, x/D
1.0	$8 \cdot 10^4$, 10^5, $1.2 \cdot 10^5$	-20 to + 20	1, 2, 3, 4, 5
0.68	10^5	-20 to + 20	1.8, 3.3, 4.8, 6.3, 7.8
0.35	10^5	-20 to + 20	3.8, 6.7, 9.6, 12.5, 15.3

Force measurements were performed on the NACA 0012 airfoil. The airfoil was suspended between two force balances to reduce reaction bending moments (Figure 2a). The lower force

balance is pictured in Figure 2. Lift and drag were measured using two SM-10 linear load cells made by Interface which were positioned 90 degrees. To eliminate friction from the force balance, each load cell was mounted on linear air bearings (New Way Air Bearings, 0.75 in bushings). Pitching moment about the quarter-chord was measured using a RTS-100 torque transducer by Transducer Techniques. Each force balance was custom built to measure time-averaged aerodynamic forces. The angle of attack of the airfoil was adjusted using a pitching mechanism consisting of an aluminum disk attached to the airfoil spar. Data was collected in 1 degree increments as the airfoil incidence was varied between ± 20 degrees.

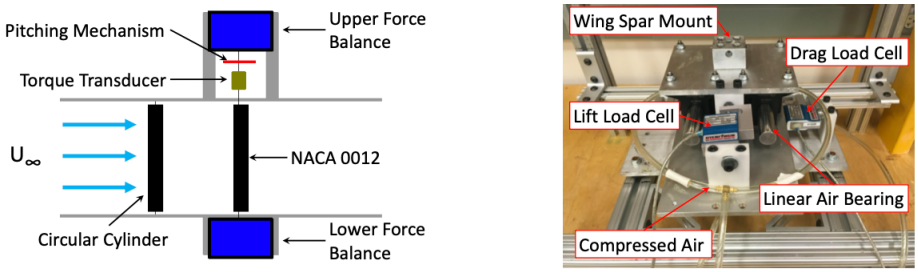

Figure 3: Schematic and picture of force balance.

The experimental investigation commenced with an analysis of the wind tunnel test section turbulence using particle image velocimetry (PIV). The PIV configuration include a double-pulsed Nd:YLF laser (Litron LDY304, 30 mJ/pulse, 10kHz maximum) with a Phantom V641 high-speed camera (4 megapixels, 1450 frames per second maximum). Reynolds numbers from 100,000 to 165,000 (250 RPM to 400 RPM) were analyzed for velocity and turbulence perturbations spatially and temporally through Fast Fourier transform analysis. Results were satisfactory for larger spatial scales, but as the field of view in the laser system was reduced to capture the temporal and smallest spatial scales of turbulence intensity, the PIV system was unable to converge and resolve these scales. These initial data were used to aid in a qualitative assessment of the numerical assessments, but the decision was made to switch to a higher resolution measurement system.

Time-averaged force measurements were acquired over 30 seconds at a sampling rate of 10 kHz using a National Instruments USB-6341 data acquisition card. The accuracy of lift, drag, and pitching moment measured by the force balance is within 1% of the total applied load. Flowfields of the cylinder-wing were obtained from time-resolved, two-component particle image velocimetry (PIV). Two high speed cameras imaged the flow at 725 Hz as a doubled-pulsed Nd:YLF laser illuminated atomized mineral oil seeding particles. To obtain the desired field of view, the cameras are tilted with respect to the laser sheet as shown in Figure 4. A Scheimpflug adapter was fitted to each camera ensuring uniform focus as the camera is tilted. A more detailed presentation of this experimental setup, including PIV processing parameters, is provided in Lefebvre and Jones.[5]

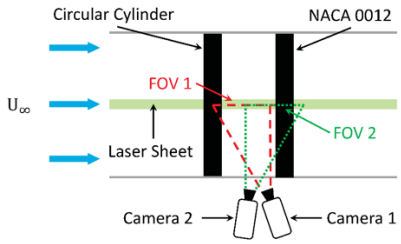

Figure 4: Sketch of PIV Setup

An IFA300 constant temperature anemometer (CTA) system from TSI Inc. provided a sampling frequency up to 300 kHz for point measurements. Using this diagnostic technique provided a broader frequency spectrum for analyzing dominant frequencies from flow features, enabling resolution of much higher temporal scales than was possible using PIV. The IFA300 includes a built-in signal conditioner capable of improving signal-to-noise ratio. ThermalPro XP software by TSI Inc. permits automatic computer control during data acquisition as well as automatic control of the traverse system and calibration procedure.

The traverse system used can evaluate up to a 33 in. displacement in two orthogonal directions, giving the capability to measure a planar section normal to freestream flow. Figure 5 shows a picture of the traverse system mounted on top of the wind tunnel test section. To obtain two velocity component measurements, an X-probe model 1150 was used. Figure 5 Figure 6 depicts the X-probe installed in the wind tunnel test section and incoming freestream. The hot-wire anemometry was applied to perform a characterization of the wind tunnel turbulence. In order acquire data, the probe must be calibrated with respect to reference velocities providing a relationship between voltage across the probe and flow velocity. To obtain an accurate reference velocity for the hot-wire probe calibration, a pitot-static system was connected to a differential CPT6100 Mensor transducer with a rated accuracy of 0.01%.

Figure 5: Traverse system used for CTA

Figure 6: X-probe for hot-wire anemometry

Computational Methodology

Numerical analysis commenced with modeling the UMD wind tunnel (Figure 7) in a structured mesh for analysis within GTSim[6], as well as with comparative results in a well-known solver, OVERFLOW. LES, hybrid RANS-LES, DES, and URANS are being used to model the wind tunnel, from the inlet screen to the expansion section to evaluate the ability of different meshes and time scales to capture the background wind tunnel turbulence. Results indicated that viscous wind tunnel walls are needed, as the typical inviscid wall assumptions in CFD are too disruptive, as illustrated in Figure 12. In addition, unsteady effects are observed from the inlet compression to the test section, so that the assumption of a steady test section inflow is not appropriate. The numerical velocity distributions are qualitatively similar to the initial PIV assessment of the tunnel; quantitative correlations will be made with the hot wire results.

The computational simulations for this study focused on the wing at zero angle of attack as all of the relevant effects of the interaction between the cylinder wake and the wing were present at all angles of attack. By focusing on the symmetric case, the results help isolate the airloads related to the unsteady wake. The dynamic analysis required relative motion between the wing and cylinder, so these simulations were performed with NASA's overset grid CFD solver OVERFLOW. The mesh consisted of the entire wind tunnel, with overset grids for the cylinder and wing, and with an extra region of refinement in the wake, as illustrated in Figure 8. Varying levels of grid refinement (Table 2) were evaluated, bracketed by meshes with approximately 161 million cells for the baseline mesh, and 217 million cells for the refined mesh. All of the increasing mesh sizes were added in the wake refinement region and the cylinder and wing grids to evaluate the scales of interest in the wake. Figure 9 shows a close up view of the test section in the x/D=2 configuration.

Table 2: Grid dimensions (streamwise, spanwise, normal) for the simulation meshes.

Refinement Level	Tunnel Background	Cylinder	Wing	Wake Refinement
Baseline	(1064, 190, 349)	(499, 190, 200)	(697, 190, 200)	(700, 190, 350)
Fine	(1064, 190, 349)	(749, 190, 250)	(997, 190, 200)	(1000, 190, 450)

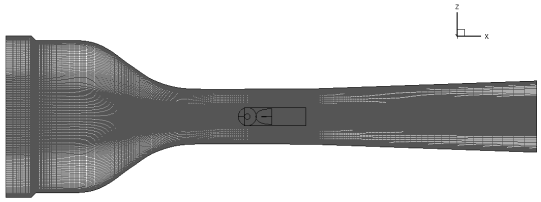

Figure 7: Top-down view of the overset CFD mesh.

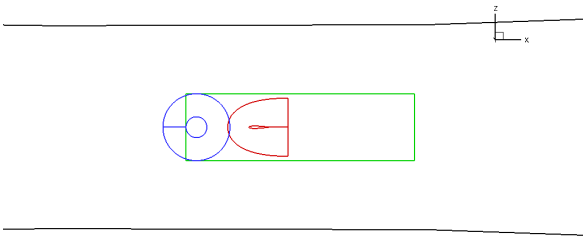

Figure 8: Tunnel (black), cylinder (blue), wing (red), and wake refinement (green) mesh outlines.

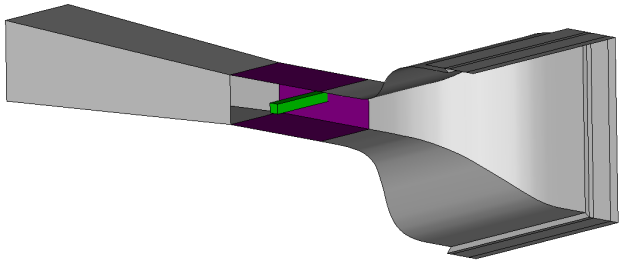

Figure 9: Example of the circular cylinder within the numerically modeled wind tunnel.

Unless otherwise noted, for all computations, the diagonalized Beam Warming flux scheme with fourth-order central differences were applied in the dynamic simulations. GTsim evaluations included uRANS, hybrid uRANS-LES, LES and DNS evaluations. OVERFLOW computations were performed with the Spalart-Allmaras (SA) one-equation turbulence closure with Delayed-Detached Eddy Simulation (DDES). Since OVERFLOW does not have an incompressible path, unlike GTsim, low Mach preconditioning improved convergence characteristics at the low speeds that were evaluated. Boundary conditions comparable to the static simulations were applied for consistency. Temporal resolution 46.4 kHz was evaluated, yielding 64 time steps per each experimental PIV image and about 750 time steps per vortex shedding cycle for a Strouhal number of 0.2. Newton subiterations ensured at least a two-order magnitude convergence between time steps. The static configurations were simulated with both meshes and compared to the experimental results to validate the mesh and modeling strategy, and the refined mesh was utilized for the static simulations.

Results

Empty Wind Tunnel Turbulence

Turbulence intensity in the wind tunnel was found to closely match the expected value and vary little with Reynolds number. Fast Fourier transform analysis of experimental PIV showed no dominant frequencies, but was not suitable for measuring temporal scales of turbulence. In addition, the PIV approach was not able to achieve convergence for the smallest spatial scales, further justifying the move to measurements with hot-wire anemometry. Hot-wire calibration was performed at the center of the wind tunnel, as the reference velocity was known at the center of the test section by the calibration curve shown in Figure 10, and the calibration in Figure 11. Turbulence intensity was measured to be 0.4% in the test section via hotwire anemometry for a freestream velocity of 22 m/s.

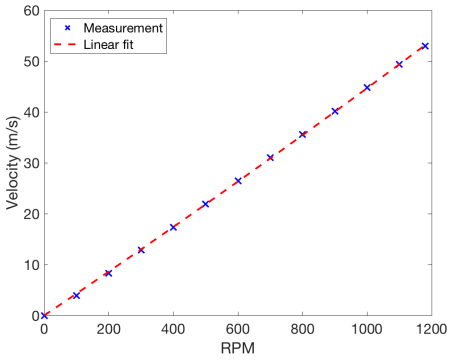

Figure 10: Wind tunnel calibration

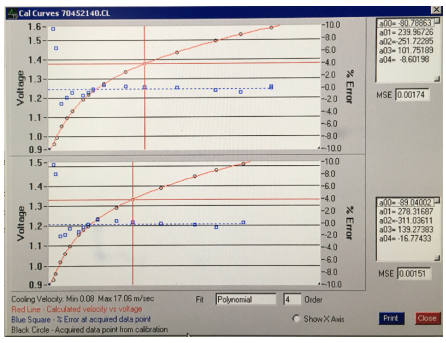

Figure 11: Calibration curve obtained for X-probe

While the CFD provided qualitative results similar to the wind tunnel data, findings indicated that current CFD practices may not be sufficient to capture wind tunnel effects. The assumption of the inviscid wall and steady inflow at the test section do not replicate the baseline wind tunnel test section. Therefore, the GTsim exploratory simulations were performed with viscous wind tunnel walls, which provided more accurate predictions. Computational analysis of wind tunnel experiments is an ongoing effort within NATO AVT-338, of which the PI is participating.

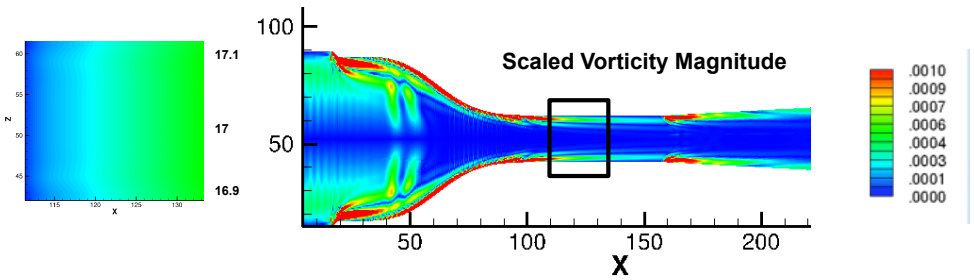

Figure 12: Example of a numerical evaluation of the empty wind tunnel turbulence levels (DES).

Static Wing Behavior Aft of a Cylinder of Reference Diameter 1

The cylinder-wing separation distance, *x/D*, has a significant influence on the airloads observed by the wing and the behavior of the flowfield around the cylinder. A subset of these results where the *D/c*=1 and Re_D=10^5 were computationally investigated to evaluate the effect of cylinder-wing separation distance in static configurations and to validate the computational approach's ability to model these interactions. For this configuration, both computations and experiments observed a change in cylinder's wake behavior when the wing was positioned between 2<*x/D*<3, characterized by a change in wing force trends and cylinder vortex shedding frequency. The static experimental data served as a validation of a high-fidelity computational solver's ability to capture the details of the static configurations, first reported by the authors in Lefebvre et al.[7] and extended with improvements to the initial correlations.

Figure 13 illustrates time averaged lift (left), drag (center), and pitching moment (right) measurements versus angle of attack from the experimental results, from the case *D/c*=1 with Reynolds number 1 x 10^5. For reference, a black curve is shown on each plot representing the wing with no cylinder present in the tunnel, hereafter referred to as the clean inflow configuration.

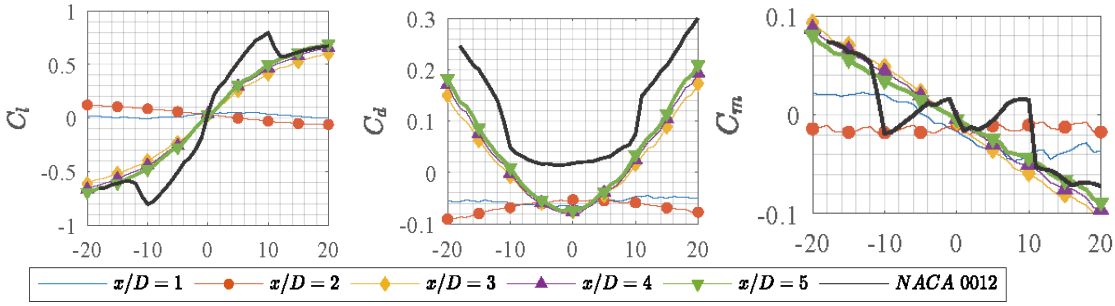

Figure 13: Time-averaged experimental lift, drag, and moment coefficient versus angle of attack (degrees) for various cylinder-wing distances at Re_c=1 x 10^5 and D/c=1.

Two distinct regimes are apparent in the force trends on the wing. For *x/D*>= 3, the time averaged lift increases with angle of attack, the drag has a minimum at zero angle of attack and is negative for low angles of attack, and the pitching moment decreases linearly with angle of attack. For *x/D*<= 2, the aerodynamics are relatively constant with angle of attack. The time-averaged lift is zero for all angles of attack, and the drag is negative for all angles of attack. This was also confirmed computationally; time-averaged drag was extracted from the static computational results and are compared in Table 3 with experiment. The cylinder wake and wing are aerodynamically coupled when *x/D*<= 2, resulting in force trends that differ significantly from the wing in a standard inflow. This behavior weakens when the cylinder and wing have a larger separation distance.

Table 3 Time-averaged drag coefficients at α=0º for the baseline and fine CFD meshes

Grid	*x/D=2*	*x/D=3*
Baseline	-0.058	-0.035
Fine	-0.065	-0.071
Exp	-0.055	-0.07

An explanation of these force trends can be identified by analyzing the flowfields in the cylinder wake. A comparison between the experimental PIV images (left) and computational results (right) is illustrated with vorticity contours in Figure 14. Regions in the experimental images (lef) that are not colored correspond to undefined data caused by laser shadows from the cylinder and wing. The mounting holes in the acrylic plates create erroneous areas of cross-correlation near the lower side of the cylinder. The overall flowfield measurements are not affected by the errors in these regions and can be used to validate CFD results. In return, the CFD can fill in gaps and provide insight into other regions of the flowfield. This emphasizes the benefits of combining the numerical and experimental analyses to develop an understanding of the flow physics. In both cases the character of the wake is captured well by the CFD simulations.

In the near wake of the cylinder for *x/D*=2 (Figure 14a), the flow separates near the top of the cylinder at *x*=-0.5, *z*=0.5. The experimental wake is characterized by a large region of recirculation inside of strong shear layers. There are large, persistent vortical structures that completely surround the wing and create reverse flow on the top and bottom surface.

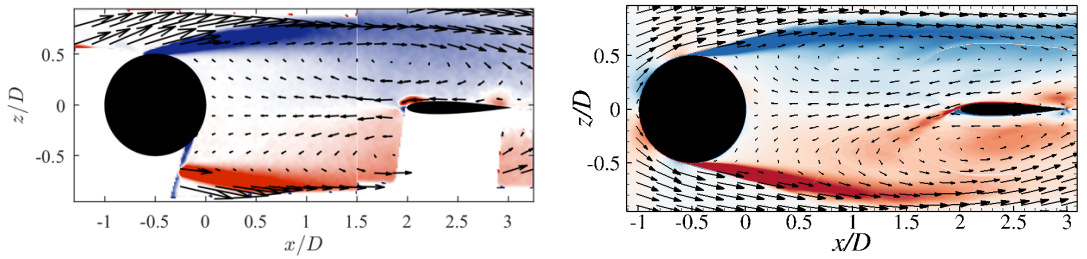

a) α=0º, *x/D* = 2

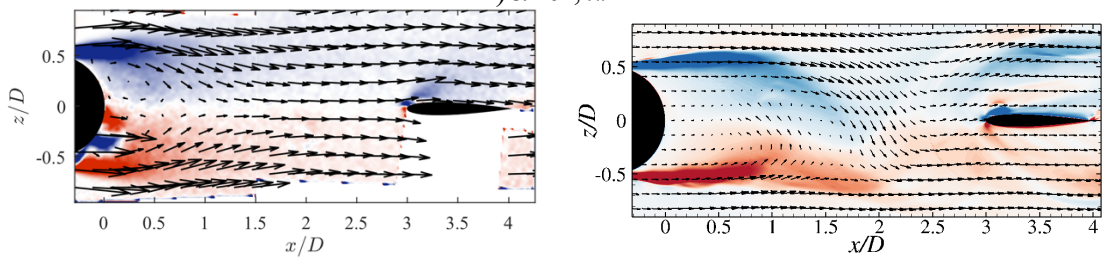

b) α =0 º, *x/D* = 3

Figure 14: Experimental (left) and computational (right) results for time-averaged flow fields for the cylinder and static wing. The computational simulations applied the fine mesh at a time step 64 times the PIV frequency.

The wake of the cylinder for *x/D*=3 in Figure 14b, shows that in both the experiments and the CFD, shear layers are no longer coherent downstream of the cylinder (*x/D*=0), and they form vortices that create a small region of recirculating flow behind the cylinder. In the time averaged flowfield, there is no reverse flow on the surface of the cylinder, but the time averaged drag is still negative. There are small regions of strong vorticity near the leading edge of the wing, suggesting that a vortex is forming there due to flow separation. This is illustrated in Figure 15, where flowfield oscillations cause a large oncoming flow angle and flow separation on the wing, which

generates a leading-edge vortex (LEV) on the wing. This creates reverse flow on the top surface of the wing, which offers an explanation for the negative drag observed.

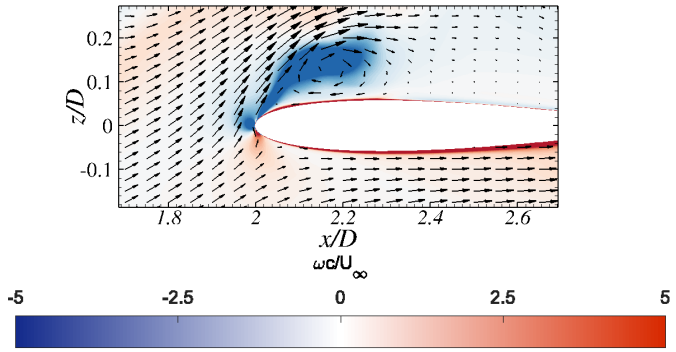

Figure 15: Time resolved snapshot of wing at x/D=3 showing LEV forming due to flow separation caused by large effective flow angle.

The shedding behavior can be analyzed by utilizing the phase-averaged flowfield for *x/D*=3, illustrated in Figure 16. For both experiments and computations, a counter-clockwise vortex is observed being shed from the cylinder at ϕ=0°. Then, as this vortex advects downstream, a clockwise vortex begins to form on the top side of the cylinder. By ϕ=180°, this vortex sheds and the phase average is a mirror image of the flowfield at ϕ=0°, demonstrating that a full cycle of the flowfield consists of the shedding of two vortices, one counter-clockwise and one clockwise.

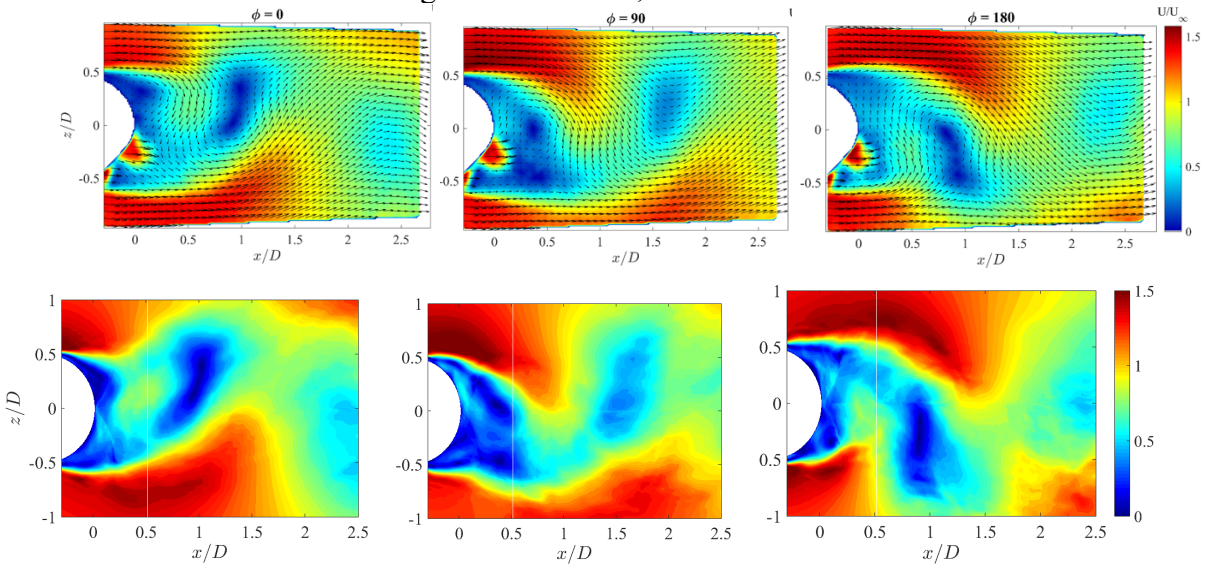

Figure 16: Experimental (top) and computational flow fields during a vortex shedding cycle (ϕ).

A fast Fourier Transform (FFT) frequency analysis of the experimental force measurements reveals the 20, 35, and 42 Hz dominant vibration modes of the cylinder by analyzing the response to a tap test. The dominant peak in the experimental lift measurements occurs at 45 Hz and 60 Hz for *x/D*=2 and *x/D*=3, respectively, which are separate from the peaks from the structural response. These dominant frequencies are associated with the vortex shedding from the cylinder and correspond to Strouhal numbers of 0.15 for *x/D*=2 and 0.2 for *x/D*=3, respectively. The shedding from *x/D*=3 agrees with previous cylinder wake studies,[8,9,10] from which a Strouhal number of about 0.2 is expected for Re_D=1 x 10^5. Similar frequencies were determined from the integrated computations. An advantage of the computational analysis is that there is no structural response,

which asserts that all of the frequencies observed correspond to flow events. However, the length of the computational data array is less than that of the experiment, so that the FFT does not have as rich of an input data set. The FFT of the lift coefficient for x/D=2 and x/D=3 each exhibit a single peak at frequencies of 43 Hz and 57.5 Hz, respectively, both about 2 Hz below the experimental measurements. The analysis of the smallest time step produced peaks at 50 Hz and 65 Hz for x/D=2 and x/D=3, respectively. Thus, the experimental data results lie between the computational data, providing a sensitivity of these frequencies. The change in shedding frequency between the two cylinder-wing distances is characteristic of the change in the flowfield character. This frequency shift provides supporting evidence of coupling between the cylinder and wing, suggesting that it is not only the wing that is affected by the separation distance, but the shedding from the cylinder is affected by the presence of the wing, and this effect is highly dependent on relative distance between the two bodies.

Dynamic Wing Behavior Aft of a Cylinder of Reference Diameter 1

After identifying a strong relationship between the behavior of the flowfield and relative cylinder-wing position, x/D, a natural extension is to investigate the effect of relative motion by moving the wing into the wake. There was no experimental counterpart to this analysis, but the experiments provide a baseline for correlation and validation. The computational approach was extended to include relative motion between the bodies to characterize the wake behavior when the wing approaches the cylinder at different speeds. This cylinder-wing analysis serves as a canonical study of these scenarios to determine the important physics that can drive modeling and simulation, as well as inform future analyses of regions where additional insights may be needed. The dynamic simulations focused on the case with the largest cylinder (D/c=1.0). There were no specific vehicle and bluff body configurations identified for this study, and these configurations and flight approach speeds are expected to vary significantly depending on the application. Thus, a notional set of wing approach speeds was identified, based on the cylinder vortex shedding to bracket the behaviors expected to dominate the flowfield coupling. For the dynamic simulations, the wing was evaluated as it moved from $5 >= x/D >= 1$ for three different wing flight speeds. The cylinder remained static. The wing speeds were selected so that the medium speed corresponded to the wing traveling one diameter per vortex shedding cycle. The lower and upper bounding speeds were one-half and twice the middle speed, respectively. These resulted in speeds of 2.19, 4.38, and 8.76 m/s, which are referred to as Cases 1, 2, and 3.

The lift and drag coefficients of the wing as it moves from x/D=5 to x/D=1 are compared for the different wing speeds. The lowest speed defined in Case 1, exhibited similar behavior to the static simulations and experiments. The trend in the lift oscillations from the experiments can be obtained from the root mean square (RMS) of the lift time history for $\alpha=0^o$. In the uncoupled regime, the RMS lift increases with decreasing gap distance, from 0.71 to 0.88 as the wing is placed from x/D=5 to x/D=3 at zero angle of attack. At x/D=2 the RMS lift is 0.68, indicating that the flowfield is coupled. The static experiments and CFD provide a reference for interpreting the dynamic results, which begin with the lift during the wing approach in Figure 17. The lift trend for the lowest speed case agrees with the static experiments. The lift oscillation amplitude increases steadily until x/D=2, at which time the amplitude decreases by 31%. For the higher approach speeds examined in Cases 2 and 3, the lift oscillations increase in amplitude throughout the flight distance examined, suggesting that the aerodynamic coupling is delayed or mitigated by the motion. The drag oscillations at the lowest flight speed increase in amplitude about a decreasing

mean value until *x/D*=2, when it changes to small oscillations about a constant mean of C_d=-0.05 (Figure 18). This average drag in the coupled regime is consistent with the static experiments. For the higher flight speeds, the drag oscillates with a constant amplitude about a decreasing time average until x/D=1, again indicating that the aerodynamic coupling has not occurred.

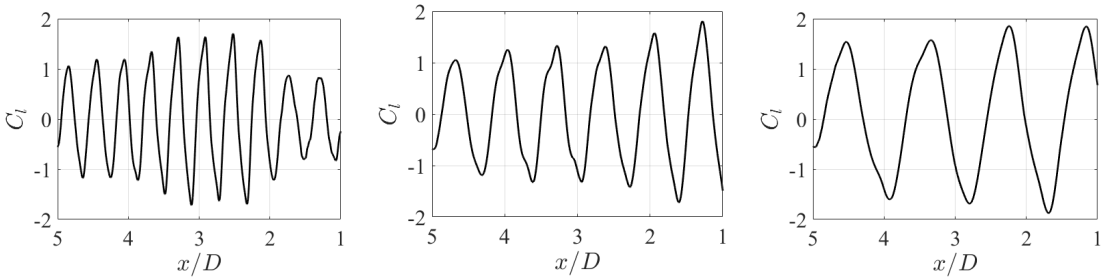

a)V=2.19 m/s *b) V = 4.38 m/s* *c) V = 8.76 m/s*

Figure 17: Wing lift coefficient for 5>=x/D>=1 at different approach speeds.

Although the aerodynamic coupling does not appear to occur at higher flight speeds based on the wing aerodynamic behavior, the cylinder wake behavior is modified for all three approach speeds analyzed, as observed by the changing amplitude of the cylinder lift between *x/D*=2 and *x/D*=3. This change correlates to the wing approach speed. For the slowest wing approach speed, the cylinder lift oscillations decrease in amplitude as the wing reaches *x/D*=2, but these oscillation amplitudes increase as the approach speed increases (Figure 19). This suggests that the shedding becomes more intense as wing approaches at these higher flight speeds.

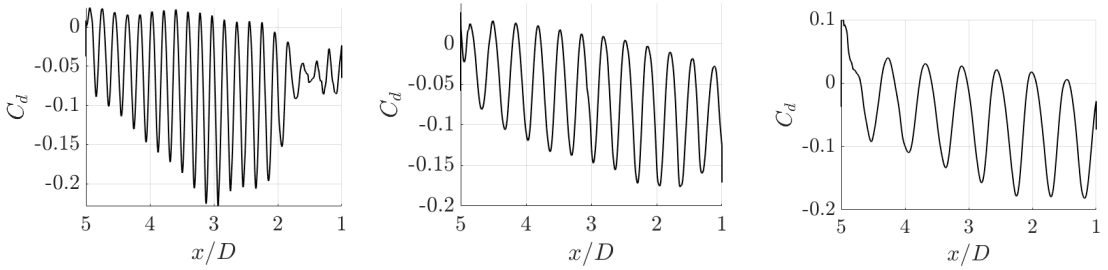

a)V=2.19 m/s *b) V = 4.38 m/s* *c) V = 8.76 m/s*

Figure 18: Wing drag coefficient for 5>=x/D>=1 at different approach speeds.

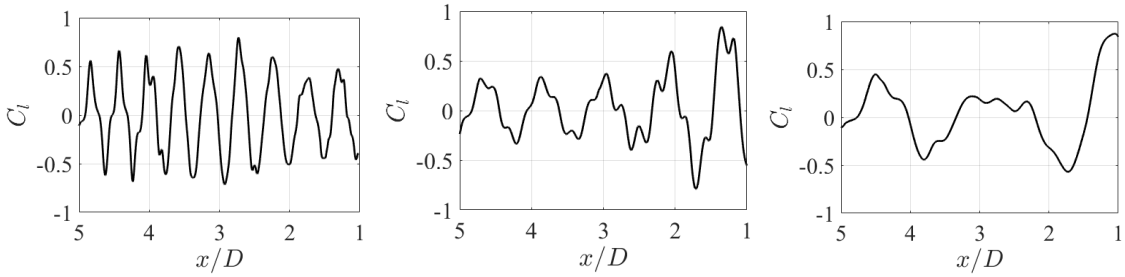

a)V=2.19 m/s *b) V = 4.38 m/s* *c) V = 8.76 m/s*

Figure 19: Cylinder lift coefficient at different approach speeds.

The frequency of the wing lift oscillations increases with increasing wing approach speed, with 76 Hz (2.19 m/s), 88 Hz (4.38 m/s), and 106 Hz (8.76 m/s). In all cases, the frequency of the lift on the cylinder is about 67 Hz, which suggests the frequency of the cylinder vortex shedding

is independent of the wing approach speed. The relationship between wing approach speed and wing lift oscillation frequency is defined by a strong linear relationship (r^2=0.9944), described by $f=4.5V_{wing}+67.0$. This shift in frequency may be explained by the Doppler effect as the wing approaches the source of the cylinder oscillations. The Doppler effect predicts a linear relationship between velocity and frequency $f = f_0\{(b+V_{wing})/b\}$ where f_0 is the shed vortex frequency and b is the velocity that the vortices propagate downstream. From this relationship, the shedding frequency of the cylinder can be recovered, and the vortex propagation velocity computed as 15 m/s. From the flowfield analysis it is observed that vortices shed from the cylinder travel about 3.1 diameters downstream per cycle. At 67 Hz this corresponds to a propagation velocity of 15.2 m/s. The wing speed and wake characteristics are closely related to the frequency of loads on the wing. This equation can be resolved to characterize the bluff body vortex shedding frequency and propagation velocity to predict the oscillations that the aircraft will encounter. This will aid in the development of operational procedures.

To gain insight into the physics, images of the flowfield were analyzed for the three approach speeds. First focusing on the uncoupled regime, the wake velocity field as the wing moves from x/D=5 to x/D=3 is illustrated for the middle speed (Figure 20). The wake structures remain consistent as the wing moves from x/D=5 to x/D=3. As vortices advect downstream, they dissipate, which concurs with the amplitude decrease in the wing lift the farther its distance from the cylinder. Similar to the static simulations, flow separates over the leading edge of the wing when the flow angle induced by the shed vortices becomes large, creating a LEV that generates reverse flow on the surface of the wing. The flowfield behavior is consistent for all approach speeds.

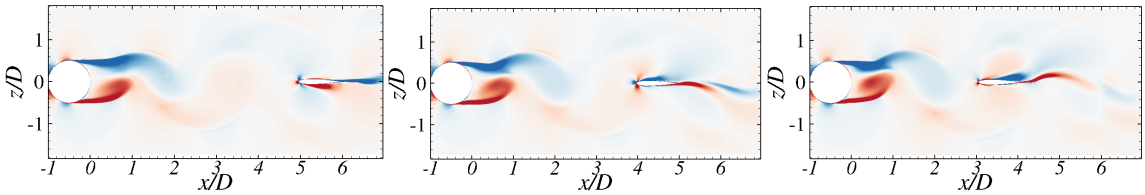

a) x/D=5 b) x/D=4 c) x/D=3

Figure 20: Time-resolved image of computationally predicted cylinder-wing interactions at wing approach speeds of 4.38 m/s (center).

The cylinder wake evolution as coupling occurs provides insight into the behavioral differences observed in the wing airloads. Figure 21 shows contours of velocity magnitude as the wing approaches the cylinder near wake (x/D <= 2) for the three different approach speeds. The wake for all flight speeds are similar when the wing first approaches x/D=2, but by the time the wing reaches x/D=1, there are noticeable differences between the different flight speeds. In the low-speed case, shedding has stopped from the cylinder and the wake begins to surround the wing, which is the signature of the coupled wake from the static configurations.

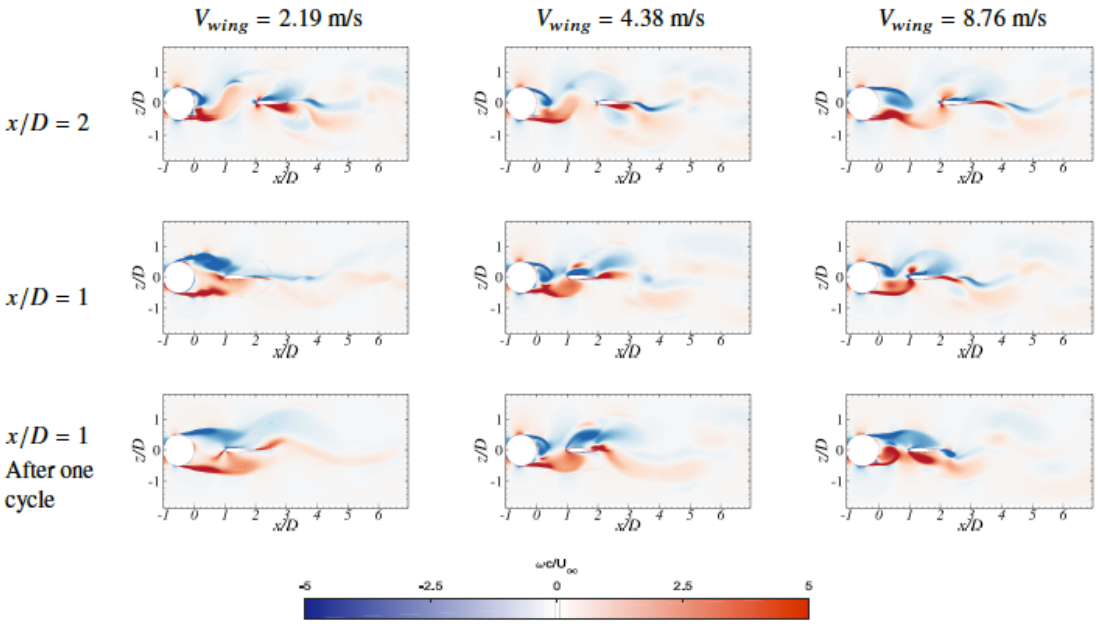

Figure 21: Time-resolved images of computationally predicted cylinder-wing interactions at wing approach speeds of V=2.19 m/s (left), 4.38 m/s (center), and 8.76 m/s (right).

Effect of Cylinder Diameter

The experimental study by Lefebvre and Jones[5] demonstrated that the lift of a wing of chord, *c*, in the wake of a cylinder is invariant to the change in cylinder diameter size, *D*, for static orientations where $1/3 < D/c < 1$. Computational analyses confirmed these findings.

Identification of the Flowfield Features for Accurate Computations

Traditional analysis of the computational solutions was determined to be too onerous to identify when computations are sufficient to capture the physics of the flowfield, as the variables of interest will "converge" differently with the various turbulence closures, time steps and mesh sizes. As an alternative, the employment of data mining techniques, such as proper orthogonal decomposition (POD) and the Sparse Identification of NonLinear Dynamics (SINDy) [11] algorithm can be applied to identify the underlying dynamics of a system by computing a sparse regression problem. The SINDy algorithm seems more adapted to this problem as it has been widely used in fluid dynamics problems where nonlinearities are ubiquitous. Furthermore, performing this model identification requires a reduced-order modeling as a fluid dynamics problem is high-order model. Several spectral analysis methods enable to reduce the order of a problem. Both the Proper Orthogonal Decomposition (POD)[12,13] and the Dynamic Mode Decomposition (DMD[14,15] are techniques used in fluid dynamics to reduce the order of a system. While the Dynamic Mode Decomposition is based on the Koopman operator to perform the spectral analysis, the Proper Orthogonal Decomposition uses the singular value decomposition. The local reduced-order bases[16] is another spectral analysis

method suited for problems characterized by different physical regimes, parameter variations, or moving features such as discontinuities and fronts. Proper Orthogonal Decomposition has been chosen to reduce the order of the fluid dynamics state as it is directly linked to turbulent kinetic energy of the system - the first POD modes contain most of the turbulent kinetic energy of the system.

A paper including these results is under preparation; the inability to work with a student (unfunded in this research) during the pandemic hampered progress, but it will be submitted in Fall 2021 now that in person research is permitted. The paper provides the code development explaining the mathematical equations for these flow cases, providing a best practice to extract numbers of planes for analysis (10, 50, 100, 500, 1000 iterations). A prior analysis of the flow past a cylinder using POD data provides validation to ensure that the SINDy and POD methods are implemented correctly. The influence of the sparsification factor and the decreasing energy captured by the POD modes is provided, followed by analysis of the data from the computations. From these analyses, it appears (at present) that the DDES and hybrid uRANS-LES with an additional length equation provide sufficient responses using meshes of the order of 5% of the airfoil chord. Correlating different cases requires that the results be time-matched to the point of oscillation in the computation, an additional step in the analysis, as illustrated in Figure 23.

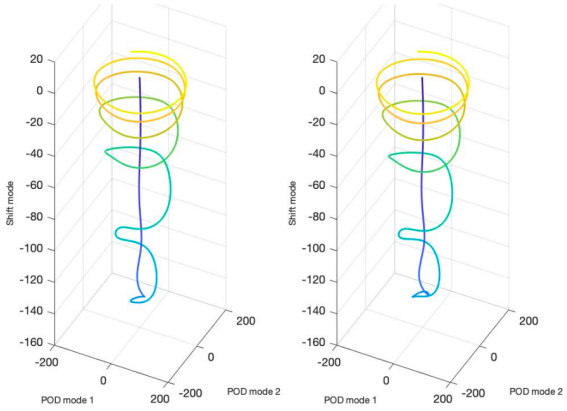

Figure 22: Comparison of the first two POD modes for a wing in the wake of a cylinder. Left is the analysis from Brunton et al.[11] compared with the results from a DDES-computed case using the present cylinder-wing configuration (right).

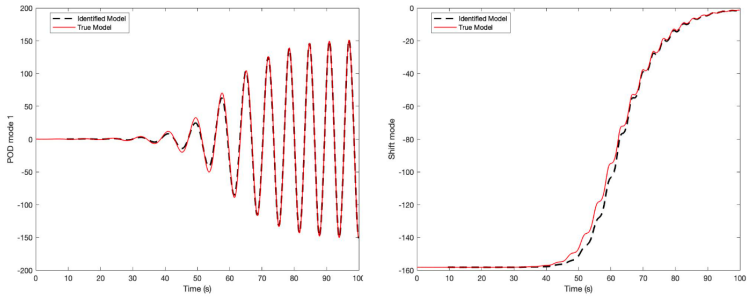

a) POD mode 1 b) Shift mode

Figure 23: Comparison of the first POD mode and shift mode for a wing in the wake of a cylinder using different meshes.

Conclusions

This research investigated the behavior of wings in the wake of bluff bodies by combining results from wind tunnel experiments and high-fidelity, time-accurate computational simulations of a semi-infinite NACA 0012 rectangular wing downstream of a cylinder. These analyses were combined to provide insight into the behavior of the wake in various configurations and to investigate the additional physics introduced when relative motion is included. The analysis has yielded several conclusions that are important in Naval shipboard operations:

- There is a coupling between the wing and cylinder wake when they are in close proximity of two or less cylinder diameters for static conditions (e.g., comparable to a VTOL vehicle in hover). This coupling has the effect of damping the unsteady shedding of vortices from the cylinder and making the flow steadier for landing. The impact on the wing is a reduced drag and a loss of lift at changing angles of attack.
- Outside of the coupling region, the bluff body wake vortex interaction with the wing results in oscillating aerodynamic coefficients on the wing due to the changing local flow angle, creating a highly unsteady flowfield that can require additional pilot workload to maneuver through. For the static evaluations, when the cylinder-wing separation distance is $x/D >= 3$, the cylinder Strouhal number is consistent with theory, $St=0.2$.
- The cylinder-wing coupling influence on the wing does not appear at higher flight speeds, but the unsteady loading on the cylinder is still present. The change in frequency of oscillations felt by the wing can be approximated by the Doppler effect, which opens the ability of its incorporation into flight control algorithms. The impact of the wing on the cylinder indicates that flight paths should avoid the regions around the ship superstructure. While these are not part of shipboard operations for larger vehicles, the design of flight paths of unmanned aerial vehicles on smaller Navy vessels could be impacted, and the operational design should maintain at least 3-5 diameters separation between the vehicle and superstructure.
- Flight speed changes in the near wake of the bluff body can result in significant transients in the aerodynamic behavior of the wing. These transients are more pronounced at higher flight speeds that do not induce the cylinder-wing coupling. This implies that vehicles who must perform near vertical take-off and landing in the wake of the superstructure should slow their speed prior to entering the region where coupling occurs to mitigate these transients.

- Computational analyses were able to predict the aerodynamic loading and wake behavior when sufficient care was taken.

Improved understanding of these effects and the relevant parameters can help design guidelines and envelopes for safer flight maneuvers for shipboard and urban canyon maneuvering of vehicles of varying sizes.

Recommendations for Future Work

Discussions with Dr. Polsky at NAVAIR has led to mutual interest in a backward facing step, which mimics some landing decks, and which will have a more complex interactional flowfield than the circular and rectangular cylinders.

In addition, a new approach to develop reduced-order, simplified models of these interactions is proposed, a vortex-impulse method, which would permit the extraction of these interactional behaviors so that the appropriate wing response can be modeled in flight simulations.

Publications Resulting from this Effort

Selected results are presented in this report, and additional publications on the topic by the authors can be found in Refs. 5, 7, 17, 18, and 19.

Acknowledgements

This ONR research supported the following graduate students to obtain their degrees: Jonathan LeFebvre, UMD (received PhD in August 2020) and Lucas Jarman, GIT (MSAE in May 2019). These students were supported by one or more semesters to provide information after the graduation of the GIT student: Amanda Grubb, GIT (PhD planned for December 2021) and Taofiq Amoloye, GIT (received PhD in August 2020).

The authors would like to thank the University of Maryland and the Ann G. Wiley Dissertation Fellowship for additional support of Jonathan Lefebvre.

In addition, the authors would like to thank the following students at the Georgia Institute of Technology who supported this effort through graded research projects (not funded under this effort): Pierre Cappe (received MSAE in May 2020) and Taylor Boyett (BSAE).

The computational team would like to thank the Office of Naval Research for the computational resources provided through the DoD High Performance Computing Modernization Program (HPCMP), S/AAA Ms. Odessa Murray.

References

1 Polsky, S., "A Computational Study of Unsteady Ship Airwake," 40th AIAA Aerospace Sciences Meeting and Exhibit, AIAA 2002-1022, Reno, Nevada, 2002. doi:10.2514/6.2002-1022.

2 Rajmohan, N., Zhao, J., He, C., and Polsky, S., "Development of a Reduced Order Model to Study Rotor/Ship Aerodynamic Interaction," in AIAA Modeling and Simulation Technologies Conference, no. AIAA 2015-0907, (Kissimmee, FL), Jan. 2015.

3 Quon, E., Cross, P.A., Smith, M. J., Rosenfield, N., and Whitehouse, G., "Investigation of Ship Airwakes Using a Hybrid Computational Methodology," in Proceedings of the 70th American Helicopter Society Forum, (Montreal, Canada), May 20–22 2014.
4 Brownell, C. J., Luznik, L., Snyder, M. R., Kang, H. S., and Wilkinson, C. H., "In Situ Velocity Measurements in the Near-Wake of a Ship Superstructure," Journal of Aircraft, vol. 49, pp. 1440– 1450, Oct. 2012.
5 Lefebvre, J., and Jones, A., "Experimental Investigation of Airfoil Performance in the Wake of a Circular Cylinder," *AIAA Journal* 57 (7), pp. 2808–2818. Online June 2, 2019. doi: 10.2514/1.J057468.
6. Hodara, J., *Hybrid RANS-LES Closure for Separated Flows in the Transitional Regime*, Ph.D. Thesis, Georgia Institute of Technology, 2016.
7 Lefebvre, J., Jones, A., Jarman, L., and Smith, M., "Experimental and Numerical Investigation of Airfoil Performance in a Cylinder Wake," *AIAA Aviation Forum and Exhibit*, AIAA-2018-3232, Atlanta, GA, 2018. To be submitted to the Journal of Aircraft, 2021.
8 Bearman, P., "On Vortex Shedding from a Circular Cylinder in the Critical Reynolds Number Regime," *Journal of Fluid Mechanics*, Vol. 37, No. 3, 1969, pp. 577–585.
9 Zdravkovich, M. M., *Flow Around Circular Cylinders, Vol 1: Fundamentals*, Oxford University Press, New York, 1997.
10 Zdravkovich, M. M., *Flow Around Circular Cylinders, Vol 2: Applications*, Oxford University Press, New York, 2003.
11 Brunton, S. L., Proctor, J. L., and Kutz, J. N., "Discovering Governing Equations From Data By Sparse Identification of Nonlinear Dynamical Systems," *Proceedings of the National Academy of Sciences*, Vol. 113, No. 15, 2016, pp. 3932–3937. https://doi.org/10.1073/pnas.1517384113, URL https://www.pnas.org/content/113/15/3932.
12 Berkooz, G., Holmes, P., and Lumley, J. L., "The Proper Orthogonal Decomposition in the Analysis of Turbulent Flows," *Annual Review of Fluid Mechanics*, Vol. 25, No. 1, 1993, pp. 539–575.
13 Majda,A.J., and Harlim ,J., "Information Flow Between Subspaces Of Complex Dynamical Systems,"*ProceedingsoftheNational Academy of Sciences*, Vol. 104, No. 23, 2007, p. 9558.
14 Rowley, C.W., Mezic, I., Bagheri, S., Schlatter, P., and Henningson, D.S., "Spectral Analysis of Nonlinear Flows,"*Journal of Fluid Mechanics*, Vol. 641, 2009, pp. 115–127.
15 Schmid,P.,"Dynamic Mode Decomposition of Numerical and Experimental Data," *Journal of Fluid Mechanics*, Vol. 656, 2010, pp. 5–28. URL http://search.proquest.com/ docview/1642228553/.
16 Amsallem, D., Zahr, M.J., and Farhat, C., "Nonlinear Model Order Reduction Based On Local Reduced-Order Bases,"*International Journal for Numerical Methods in Engineering*, Vol. 92, No. 10, 2012, pp. 891–916. https://doi.org/10.1002/nme.4371
17 Lefebvre, J., *Cylinder-Airfoil Interactions and the Effect on Airfoil Performance*. Ph.D. Thesis. Department of Aerospace Engineering, University of Maryland, College Park, MD, USA. May 2021.
18 Burke, B., Boyett, T. and Smith, M.J., "Determination of the High Fidelity Computational Modeling Requirements for Complex Bluff Body-Wing Interactions," under preparation, 2021.
19 Jarman, L., Burke, B., and Smith, M.J., "Dynamic Response of a Wing in the Wake of a Cylinder," under preparation, 2021.